A Process Model for the Distortion Induced by the Electron-Beam Welding of a Nickel-Based Superalloy

H.J. STONE, S.M. ROBERTS, and R.C. REED

A process model suitable for the prediction of the distortion induced during the electron-beam welding of nickel-based superalloys is described. For the purposes of model validation, processing trials on WASPALOY have been carried out using an industrial-scale welding apparatus. Particular emphasis has been placed on the effect of altering the focal position of the beam. The heat transfer occurring during welding has been characterized, and values of the thermal efficiency are reported. The thermal cycles experienced by material in the heat-affected zone (HAZ) are reproduced accurately. The resulting modes of distortion, both angular and camber, have been analyzed. For one of the welds, the residual-stress state has been determined using the neutron diffraction technique, and it is shown that the predictions are in reasonable agreement with the observations. While there are some discrepancies, the model is capable of rationalizing the modes and extent of distortion and the manner in which these depend upon the focal position of the beam.

I. INTRODUCTION

ELECTRON-BEAM welding[1,2,3] remains an important manufacturing process, particularly in the automobile, aerospace, construction, and power-generation sectors. This is because it offers a significant number of advantages compared to other fusion welding techniques, despite its high cost. First, weld profiles of high penetration can be obtained, and this enables sections of significant thickness to be joined.[4] Second, as the processing is typically performed under a high vacuum, the likelihood of weld contamination by oxide and nitride inclusions is small, so that the welds are suitable for structural applications in which resistance to fracture and fatigue is particularly important.[5,6] Third, as less power per unit length of weld is required than for the arc-welding processes, the distortion induced in the component is often correspondingly smaller, even when thick sections are joined.[7,8] This helps to minimize the possibility of cracking and to reduce the degradation of the material properties within the weld and heat-affected zone (HAZ). Finally, the process has proved amenable to automation, and this has allowed autogeneous welds of extremely high quality to be reproduced in manufacturing environments.[9,10]

However, when electron-beam welding is the preferred joining technique, stringent limits can be placed on the levels of distortions and residual stresses that can be tolerated, often because of the intended use of the structure being fabricated. Where these are exceeded, significant extra costs can be incurred during the manufacturing cycle, since components need to be reworked or scrapped. One way of dealing with this eventuality is to build process models for the various steps in the manufacturing sequence, so that optimal sets of processing parameters can be identified before resorting to tests on the factory floor. With the arrival of fast low-cost computers and advanced computer software, the construction and application of this kind of virtual manufacturing capability is rapidly becoming possible. However, when designing such models, the desire to incorporate as much of the relevant process physics as possible must be balanced against the costs of implementation and validation and the limitations of existing computer hardware. For example, if the desired product of a welding model is to generate predictions of the shape of the fusion boundary, then consideration of the fluid flow in the melt pool alone may suffice (*e.g.,* Reference 11). On the other hand, if predictions of the residual stresses and distortion are required, then accurate predictions can be made with a more simplified description of the heat transfer to the workpiece (*e.g.,* Reference 12), with the complex phenomena that occur in the vapor cavity and the melt pool being neglected. A degree of pragmatism is desirable, since a large number of phenomena occur during the fabrication of a weld, and the modeling of all them in a single process simulation will not be possible for some years.[13,14]

In the present article, an investigation is made of the distortion induced during the electron-beam welding of a high-strength nickel-based superalloy, WASPALOY.* Particular emphasis is paid to the effect of defocusing the beam and, hence, the focal position with respect to the surface of the workpiece. A numerical model is developed which is capable of simulating the distortion and the spatial and temporal distribution of the stress states that are responsible for it. For the purposes of model validation, a number of processing trials have been carried out on an industrial-scale welding machine, which has enabled the transfer of heat to the workpiece to be quantified. The distortion and residual-stress states have been characterized using analytical techniques. As will be seen, the distortion depends strongly upon the shape of the weld pool and, hence, the manner in which this is altered as the welding parameters change.

*WASPALOY is a trademark of Precision Rings, Inc., Indianapolis, IN.

H.J. STONE, Graduate Student, S.M. ROBERTS, Rolls-Royce Research Fellow, and R.C. REED, Assistant Director of Research, are with the Department of Materials Science and Metallurgy, University of Cambridge/Rolls-Royce University Technology Centre, Cambridge, United Kingdom CB2 3QZ.

Manuscript submitted August 31, 1999.

II. BACKGROUND

It is well known that the interaction between an electron beam and the workpiece during electron-beam welding gives rise to a number of complicated phenomena. As the beam impinges upon the metal surface, the energy of the electrons is deposited in a very small depth of material, due to the limited intrinsic penetration depth of electrons into metals.[1] As with other fusion-welding processes, if energy is supplied at a rate greater than that which can be conducted into the workpiece, melting of the metal will necessarily occur. At the power densities that can be achieved with electron-beam welding, the formation of a superheated vapor is possible, and the recoil pressure generated by this vaporization on the molten metal at the base of the weld cavity forces the molten metal downward and sideways.[4] Consequently, the electron beam can impinge on the metal at the base of the vapor cavity and, hence, melt and vaporize it. This "digging" action of the electron beam allows the vapor cavity to extend to considerable depths into the workpiece surface, thus generating the vapor keyhole that is a characteristic of this welding process. For successful welding, it is important that this keyhole is maintained during processing by the complex balance of forces acting upon it (Figure 1). The pressure of the vapor and the recoil pressure from the evaporation of the metal act against the surface tension and hydrostatic head of the molten film to prevent the collapse of the cavity. Additionally, frictional forces between the liquid and the solid material act to prevent the sinkage of the molten metal down the walls of the cavity under gravity.[4] As the keyhole advances through the workpiece, the molten metal is driven to the rear of the weld pool by thermally activated surface-tension gradients, *i.e.*, the so-called Marangoni flow,[15,16] where conduction of heat to the bulk finally allows the metal to solidify. The action of the vapor pressure in the cavity also serves to drive the molten metal film out from both ends of the keyhole exposed to free space. This leads to the formation of complex topbead and underbead profiles on solidification.[17]

These considerations suggest that the shape of the weld pool should depend strongly upon the welding parameters that are employed, and this is indeed the case (*e.g.*, References 18 through 20). The parameters that may be controlled by the operator include the accelerating voltage, the beam current, and the focal position of the beam. For most applications, it is desirable to generate a weld possessing a narrow fusion zone, with sides perpendicular to the surface of the workpiece. It has been suggested[1] that increasing the accelerating voltage results in narrower, parallel-sided welds with increased depths of penetration. This is because higher accelerating voltages yield smaller beam diameters as a result of space-charging effects, and for this reason it is often recommended that welding be conducted at the maximum accelerating voltage of the system.[1] In contrast, the effects of varying the beam current or focal position on the shape of the weld pool are less well understood. Experience shows that the ranges of current and focal position which yield sound welds are rather narrow. For example, by varying the beam current, it is possible to go from (1) supplying insufficient power to the workpiece to (2) achieving full penetration and, finally, to (3) supplying too much power, thereby increasing the molten region to such an extent that it can no longer be supported by the internal vapor pressure, a situation that encourages sinkage of the weld pool.[1] Similarly, heavy underfocusing or overfocusing of the beam results in a power density that is insufficient for the formation of a vapor cavity and, in these circumstances, an approximately hemispherical weld pool forms,[2] the shape of which is governed by convective fluid flow. As the focal position approaches the surface of the workpiece, a condition that has traditionally been termed "normal focus," a vapor cavity arises as a result of the keyholing effect and the penetration increases markedly.

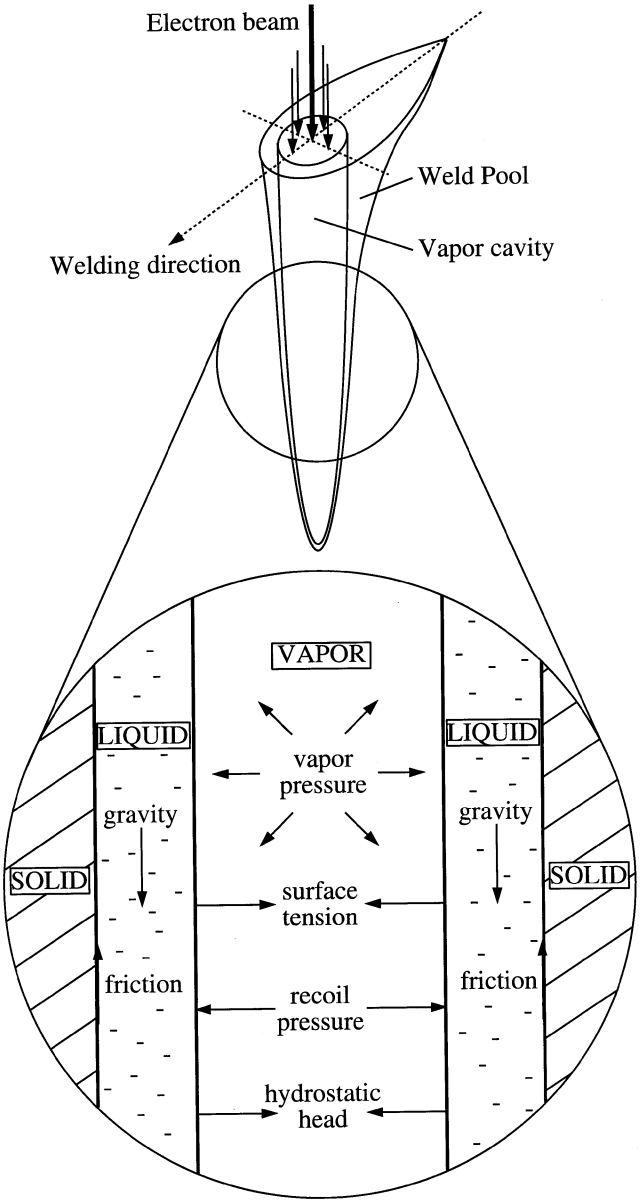

Fig. 1—Schematic illustration of the balance of forces in the vapor cavity and weld pool within a keyhole weld.

III. DETAILS OF THE EXPERIMENTATION

A. *Manufacture of the Welds*

A series of rectilinear plates of the dimensions 200 × 50 × 9 mm were machined from a WASPALOY forging, which

Table I. The Chemical Composition (Weight Percent) of the WASPALOY Material Used in the Present Study

Ni	Cr	Co	Mo	Ti	Al	Fe	W	Zr	C	Si	V	Mn	B
57.5	19.2	13.9	4.03	3.04	1.31	0.88	0.07	0.06	0.02	0.02	0.01	0.01	0.004

Table II. Welding Parameters Used for the Fabrication of the Electron Beam Welds

Voltage (kV)	Beam Current (mA)	Velocity (mm s^{-1})	Defocus (mA)	Distance from Normal Focus (mm)	Focal Plane
150	23	8.4	+90	58	above surface
150	23	8.4	+70	45	above surface
150	23	8.4	+50	32	above surface
150	23	8.4	+40	26	above surface
150	23	8.4	+30	19	above surface
150	23	8.4	+20	13	above surface
150	23	8.4	+10	6	above surface
150	23	8.4	+0	0	normal focus
150	23	8.4	−20	−13	below surface
150	23	8.4	−40	−26	below surface

was supplied by Rolls-Royce plc. The chemical composition is given in Table I. The microstructure consisted of a γ matrix (~70 vol pct) and γ' precipitates (~30 vol pct); the grain size was approximately 40 μm. Prior to welding, each plate was subjected to a heat treatment to reduce as far as practicable any residual stresses that were present. This was conducted in a vacuum furnace and involved heating the testpieces to 760 °C, followed by a 5-hour dwell and a furnace cool to ambient temperature. Measurements of the surface residual stresses remaining after this treatment were then conducted by X-ray diffraction using the $\sin^2 \psi$ method, as in Reference 21. These were found to be typically small: 60 ± 50 MPa along, and −90 ± 60 MPa perpendicular to, the grinding direction, respectively.

A Steigerwald K-100 electron-beam welding device at Rolls-Royce (Derby, United Kingdom) was employed for the welding of the testpieces. This facility allowed the automatic control and monitoring of each of the welding parameters during processing. With this kind of welding device, the process parameter controlling the focus of the electron beam is the current passing through the focusing coils; this parameter in itself provides no information concerning the focal position of the electron beam, and, hence, calibration of the focal position against the defocusing current is necessary. This was achieved by measuring the current required to achieve a normal focus at a number of positions along an inclined plate, as in Reference 1. Once this had been done, autogeneous bead-on-plate welding passes were placed along the center of each testpiece in the long direction. The welds were fabricated at ten different magnitudes of the beam defocus, which lay between the underfocused and overfocused conditions. All the remaining welding parameters were kept constant (Table II); each of the samples welded is referred to by the difference between the focusing current at which it was welded and the focusing current required for normal focus.

For the purposes of the present experiment, the testpieces were mounted on a purposely built fixture that imposed no constraint or loading other than that by gravity. This allowed the free deformation of the testpieces during welding and on subsequent cooling. Thermal isolation was achieved by inserting glass slides between the sample and fixture.

B. *Process Monitoring of Thermal Cycles*

During welding, thermal cycles were monitored by the use of four K-type thermocouples spot-welded to the surface of the testpiece, following the procedure reported in Reference 21. One of these was attached at the starting edge of the weld to determine the point of impingement of the electron beam on the testpiece. The remaining three were positioned across the center of the plate at various distances from the weld path. A schematic illustration of the prepared sample, showing the mounting positions of the thermocouples, is given in Figure 2. The measurements were extracted from the thermocouples using a shielded thermocouple extension cable. This was routed to a commercial data-capture apparatus placed outside the vacuum chamber *via* a purposely built vacuum chamber cover port. Suppression of noise in the signal was achieved by the application of input filtering.

C. *Distortion Measurement*

The weld-induced distortion was characterized using a Leitz PMM12106 three-dimensional needle-probe coordinate measurement device. This was used to trace and record the locations of the surfaces of the welded testpieces. Thus, it was possible to identify and characterize the two principal modes of distortion: (1) angular distortion, or "butterflying," which manifested itself as a bending of the testpieces about the axis of welding and which could, therefore, be characterized *via* a "butterfly angle" and (2) cambering, *i.e.*, curvature of the testpieces along the length of the weld. Schematic illustrations of these two distortion modes are given in Figure 3.

D. *Residual-Stress Measurement* via *Neutron Diffraction*

The residual-stress state in the testpiece welded at a +20 mA defocus was characterized using the neutron diffraction technique at the ISIS facility of Rutherford Appleton Laboratory (Didcot, Oxfordshire, United Kingdom). The measurements were performed at seven measurement locations across the center of the testpiece, as illustrated in Figure 4.

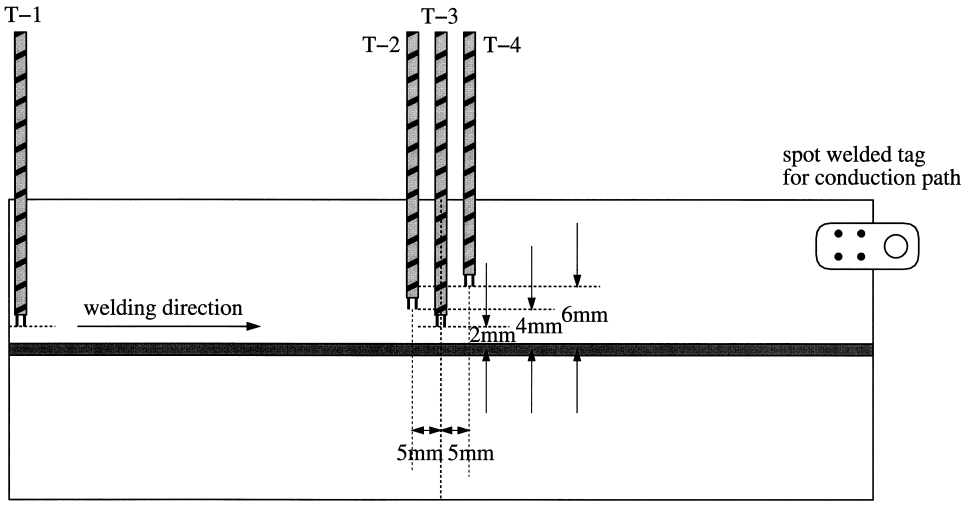

Fig. 2—Diagram of the testpiece illustrating the location of the thermocouples.

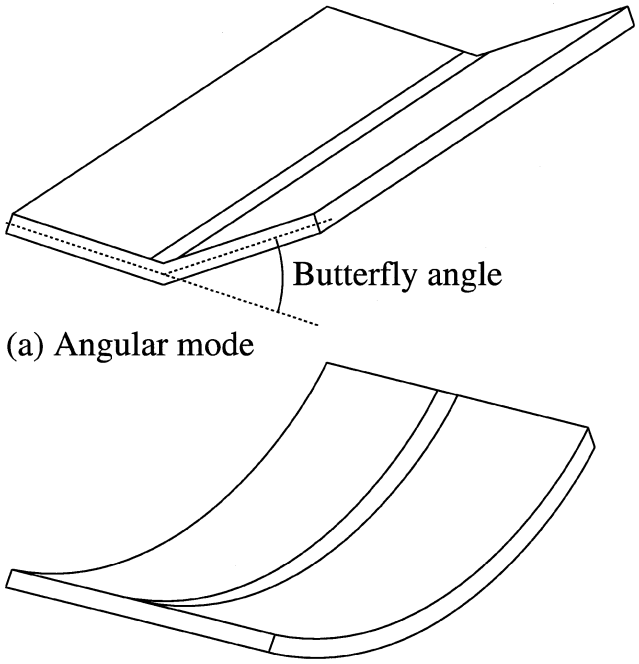

Fig. 3—Schematic illustration of the two modes of distortion considered in the present article: (*a*) angular distortion and (*b*) cambering.

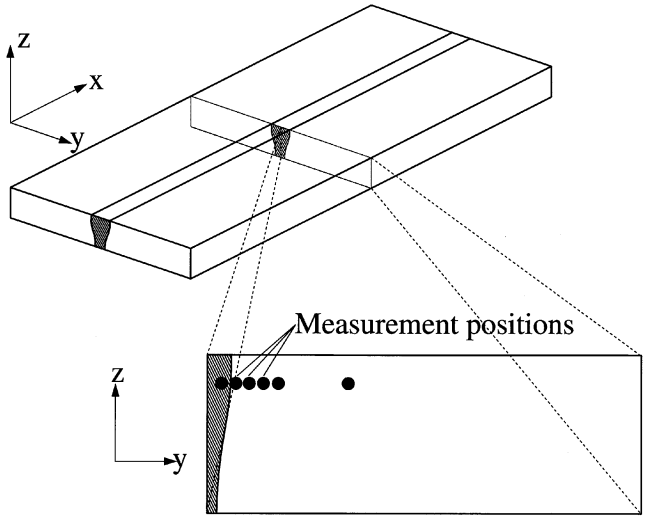

Fig. 4—Diagram illustrating the locations in the weld where residual stress determination was carried out using the neutron diffraction technique.

Spatial resolution was provided by the use of 1 × 10 mm slits in the incident beam path, which gave an illuminated gage volume of 1 × 1.5 × 10 mm. The measurements were performed at a depth of 1 mm beneath the sample surface, thus ensuring that the gage volume was fully immersed in the sample and, thus, that edge effects were avoided.

As the ISIS facility there is a spallation source, and spectra containing all lattice reflections were obtained. The resultant spectra were composed principally of the overlaid diffraction patterns generated by the γ matrix (~70 vol pct) and the γ' precipitates (~30 vol pct). However, as a result of the small lattice mismatch between these phases and the large intrinsic line widths, it was not possible to resolve the reflections into their various phase constituents. However, it is believed that the treatment of the composite diffraction pattern as a single pattern does not generate erroneous results.[22] Consequently, the average strain in the sample was obtained by performing a Reitveld refinement on each full spectrum, assuming only a single-phase fcc material. Conversion of the measured strains was then achieved using estimates of the bulk elastic modulus and Poisson's ratio.[23] It has been shown that this method provides an accurate measure of the macroscopic residual-stress state, while overcoming the problems created by the presence of microstresses in the material.[24] Three sets of measurements of lattice strain were made along directions defined by the directions of the plate; these were assumed to be the principal directions, and conversion of lattice strain to bulk residual stress was carried out as in Reference 21.

E. *Metallographical Analysis*

Metallographic sections of each of the welds were prepared in the plane perpendicular to the direction of welding, to determine the forms of the fusion-boundary profiles.

Microstructural relief was achieved using Kalling's reagent, a mixture of 5 g $CuCl_2$, 100 mL HCl, and 100 mL ethanol.

IV. NUMERICAL MODELING

A numerical model was formulated, with a view to rationalizing the modes of distortion and their magnitudes, by simulating the macroscopic transient fields of temperature, displacement, strain, and stress using the equations of continuum mechanics. The approach follows the pioneering work of Goldak and co-workers (*e.g.*, References 25 through 27), Karlsson and co-workers (*e.g.*, References 28 through 30), and Leblond and co-workers (*e.g.*, References 31 through 33). As the amount of heat generated through plastic work is negligible compared to that provided by the source,[34] so-called weakly coupled analyses were performed. Hence, the calculated thermal fields were used as the input conditions for the mechanical analyses. The computations have been carried out in three dimensions, in the Lagrangian reference frame, using the small-strain assumption.

For the purposes of the present article, the finite-element method (FEM) and the SYSWELD software code[35] have been employed. Temperature-dependent material properties have been used,[36,37] although it should be noted that no account was taken of microstructural changes arising from the passage of the beam. The temperatures within each element were approximated with linear-basis functions, *i.e.*, linear elements. To ensure that any bending of the testpiece was captured adequately, quadratic elements were chosen for the mechanical analysis. Reduced integration was used to ensure that the elastic and plastic strains were compatible with the thermal strains computed from the temperature field[27] and to prevent "volumetric locking," which can yield poor computational performance,[26] *i.e.*, overly stiff response; however, the effect /f using different different-element and integration techniques is examined in detail in Section VI.

A. *Mesh Generation*

One of the principal challenges in computational weld mechanics arises from the question of scale: the steep temperature gradients in the vicinity of the source must be simulated, but it is the distortion of the plate itself which is of interest. Following preliminary investigations, elements one-quarter the size of the characteristic heat source have been used in the vicinity of the source; thus, oscillations in the temperature field near the source were avoided. However, as the heat source is ~1 mm in diameter and is required to traverse the full 200 mm length of the model, the discretization of the plate with this size of element leads to prohibitively large computing costs.

To solve this problem, a form of adaptive remeshing has been used, in which the necessary refinement around the heat source is provided along a short section of the weld path only, with larger elements beyond. Use was made of a number of purposely built macros in the command language, although it should be noted that the source code of SYSWELD was not altered. Thus, the complete analysis involves a series of subanalyses each with its own unique mesh (Figure 5). The last set of results of each subanalysis is then interpolated on to the next mesh, and the heat source is allowed to traverse along the next refined region. With this technique, the number of elements and, hence, the computational expense was greatly reduced. A similar projection procedure was utilized for the mechanical analysis.

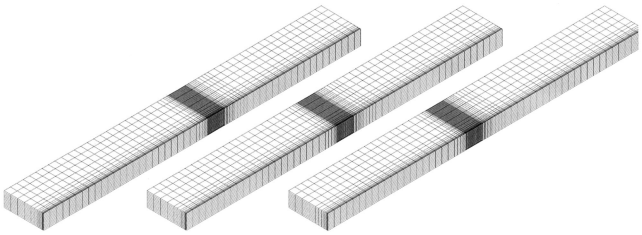

Fig. 5—Examples of the meshes used for the thermal model in three consecutive subanalyses.

B. *Thermal Model*

The primary aim of the modeling was to rationalize the distortion observed, and it is known that the volume of the zone which is plastically upset is about 5 times the volume of the metal that is melted.[21] Thus, for the present purposes, many of the transfer phenomena occurring in the weld pool are of secondary importance and, therefore, a pragmatic decision was made that a phenomenological description of the heat transfer to the workpiece would suffice.

Early analytical models (*e.g.*, Reference 38) of the heat source, which employ point or line sources, cannot be easily incorporated into FEM analyses, since singularities in the temperature exist at the weld centerline. Instead, the use of a distributed source (*e.g.*, References 39 and 40) is appropriate. During the course of the present work, a number of heat-source descriptions were assessed. Eventually, a model was chosen for the heat source which was composed of two distinct contributions: a uniform circular surface flux ($q_{surface}$, in units of W/m^2) and a uniform conic volumetric source (q_{volume}, in units of W/m^3). If the plate is of dimensions X, Y, and Z and the Cartesian coordinate system (x, y, z) is aligned with it, such that the source moves at a constant velocity (v) in the yz plane in the x direction, the two source strengths, $\dot{Q}_{surface}$ and $\dot{Q}_{volume}$, are given by

$$\dot{Q}_{surface}\{\xi, y\} = q_{surface} \text{ where } \xi^2 + y^2 \le a_{surface}^2$$
$$= 0 \quad \text{where } \xi^2 + y^2 > a_{surface}^2 \qquad [1]$$

and

$$\dot{Q}_{volume}\{\xi, y, z\} = q_{volume} \text{ where } \xi^2 + y^2$$
$$\le (mz + a_{volume})^2 \text{ and } z \le d \qquad [2]$$
$$= 0 \text{ where } \xi^2 + y^2 > a_{surface}^2 \text{ or } z > d$$

with $\xi = x - vt$, where t is the time. The terms $a_{surface}$ and a_{volume} are the characteristic radii of the two sources at the surface of the plate, m is a constant describing the conic source, and d is the penetration depth of the electron beam, which equals the thickness of the plate in the fully penetrating condition. The total power delivered by the two heat-source terms must equal that provided by the electron beam, so that

$$\eta VI = \int_{\delta\Omega} \dot{Q}_{\text{surface}}\, dS + \int_{\Omega} \dot{Q}_{\text{volume}}\, dV$$
$$= \pi a_{\text{surface}}^2\, q_{\text{surface}} + \pi d \left(\frac{1}{3} m^2 d^2 + m d a_{\text{volume}} + a_{\text{volume}}^2 \right) q_{\text{volume}} \quad [3]$$

The terms q_{surface} and q_{volume} may then be obtained by defining a partitioning ratio (r) as the proportion of the total power in the surface source. Then,

$$q_{\text{surface}} = \frac{r\eta VI}{\pi a_{\text{surface}}^2} \text{ and}$$
$$q_{\text{volume}} = \frac{(1-r)\eta VI}{\pi d \left(\frac{1}{3} m^2 d^2 + m d a_{\text{volume}} + a_{\text{volume}}^2 \right)} \quad [4]$$

The four parameters a_{surface}, a_{volume}, m, and r cannot be obtained directly from measurements; they must be chosen by comparison of the experimental information with the computed weld fusion-boundary profiles and thermal cycles.

The power delivered by the electron beam is proportional to the product of the accelerating voltage of the beam (V) and the beam current (I). However, as not all of this power is absorbed by the workpiece, it is necessary to define a coupling efficiency (η), so that an accurate measure of the total heat deposited in the workpiece can be recovered by the model. This was estimated experimentally from the observation that the plates, shortly after welding, attained a uniform temperature (T_{sat}), provided that the vacuum chamber remained sealed. Use was made of surface-mounted thermocouples, as in Reference 21. Hence,

$$\eta = \frac{vC_pY\, Z(T_{\text{sat}} - T_0)}{VI} \quad [5]$$

where C_p is the volumetric heat capacity and T_0 is the initial temperature of the plate.

C. *Mechanical Model*

The mechanical constraints imposed on the model consisted of (1) a symmetry condition on the plane containing the weld path, (2) a pin joint at one end of the plate, and (3) a simple support at the other. These constraint conditions are consistent with the experimental conditions and allow the angular and camber distortion modes to be reproduced. Transformation plasticity and microstructural evolution, while worthy of consideration for many welded materials, *e.g.*, steels, are not considered to contribute significantly to the evolution of total strain in Waspaloy. Temperature-dependent properties were used for the coefficient of thermal expansion, Young's modulus, yield stress, and hardening coefficient.[36,37]

V. RESULTS AND DISCUSSION

Examples of the cross sections of the welds are shown in Figure 6(a). Near to the condition of normal focus, an approximately parallel-sided weld is produced. However, as the electron beam is defocused, either by underfocusing or overfocusing, the weld produced becomes increasingly asymmetric. At the largest defocuses investigated (+90 mA and −40 mA), full penetration is not achieved and T-shaped fusion-boundary profiles are obtained.

A. *Thermal Analysis*

The estimates of the thermal efficiencies are given in Table III. These were made *via* Eq. [5] from values of T_{sat}, as described in Section IV–B and in Reference 21. The values vary from 97 pct for the most-defocused beams to 80 pct at the normal focus condition, when the process is at its most inefficient, since a fully penetrating weld is produced. These estimates compare favorably with those given in the literature.[1]

The heat-source parameters (a_{surface}, a_{volume}, m, and r) selected for the thermal analysis are given in Table III. It was found that these parameters were able to reproduce the experimentally determined fusion profiles with a very reasonable degree of accuracy (compare Figure 6(b) with Figure 6(a)). This was particularly true of the fully penetrating welds, which were manufactured close to the condition of normal focus. Away from the conditions of normal focus, a reasonable correlation between the fusion-boundary profiles was again observed, but it is notable that the welds were prone to occasional undercut and underbead (Figure 7). As presently constituted, the model is unable to predict these features, which arise from instabilities in the transport phenomena during processing. The formation of a weld underbead was not observed at the conditions of normal focus, however.

Since the parameters a_{surface}, a_{volume}, m, and r have been chosen from a consideration of the pool shape, comparison with the observed thermal profiles represents a better test of the thermal model (Figure 8). Here, the measured thermal cycles have been compared with those predicted, assuming an uncertainty of ±0.2 mm in the location of each thermal cycle; hence, two computed curves are plotted. Given the uncertainties associated with the thermocouple positioning, their finite width, thermal mass, and associated temperature lag, the authors believe that the agreement between model and experiment is reasonable. Thus, the thermal model is suitable for testing whether the mechanical model can predict the distortion observed.

B. *Mechanical Analysis*

1. *Comparison of measured and predicted stresses*

The variations of the longitudinal and transverse surface stresses, for the testpiece welded at a +20 mA defocus, with distance from the centerline are presented in Figure 9. The maximum stresses are in the longitudinal direction, and the magnitude of these, ~1000 MPa, is equivalent to the yield stress of the material. As discussed in Reference 21, the region that is upset plastically extends a distance ~5 mm away from the weld centerline. The agreement between theory and experiment is reasonable.

For the transverse stresses (Figure 9(b)), one can see that the agreement between theory and experiment is less good. Positive values of the transverse stresses were measured in all cases, whereas, at points equivalent to the locations of the measurements, compressive stresses are predicted at the centerline, with tensile stresses further away in the HAZ.

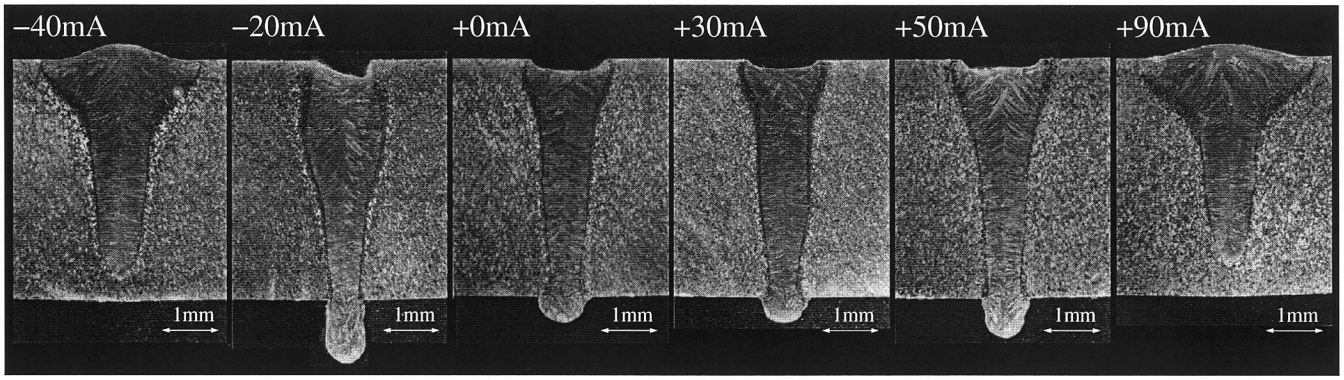

(*a*)

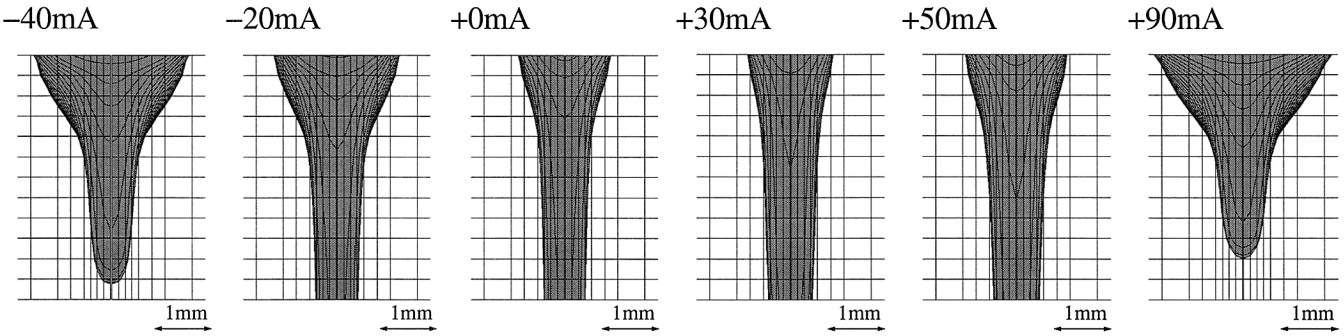

(*b*)

Fig. 6—(*a*) Photographs of the metallographic sections obtained from the testpieces welded at beam defocuses of −40, −20, 0, +20, +50, and +90 mA; and (*b*) fusion boundary isotherms obtained from the numerical model corresponding to the testpieces welded at defocuses of −40, −20, 0, +20, +50, and +90 mA.

Table III. The Heat Source Parameters and the Thermal Efficiencies Used for the Numerical Model (Equations [1] through [5])

Defocus (mA)	η	$a_{surface}$ (mm)	a_{volume} (mm)	m	r	d (mm)
+90	0.96	3.5	1.05	−0.025	0.35	7.7
+70	0.97	2.52	1.02	−0.0225	0.20	9
+50	0.88	1.76	1.0	−0.02	0.10	9
+40	0.88	1.79	1.0	−0.0175	0.10	9
+30	0.81	1.58	0.95	−0.015	0.075	9
+20	0.80	1.54	0.95	−0.013	0.075	9
+10	0.80	1.57	0.95	−0.013	0.075	9
+0	0.79	1.65	1.0	−0.015	0.10	9
−20	0.93	2.20	1.02	−0.02	0.20	9
−40	0.97	3.05	1.05	−0.025	0.30	9

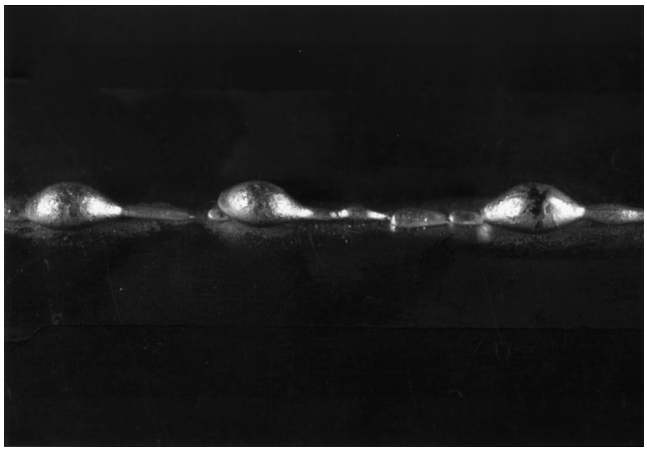

Fig. 7—Photograph of the underbead of the testpiece welded at +70 mA defocus, which showed considerable underbead and undercut.

This situation warrants some discussion, and at this point it becomes advantageous to have a model with which to compare the experimental data. An important point concerns the manner in which the state of stress varies with position within the vicinity of the weld; the modeling has shown that, while the sign of longitudinal stress does not vary through the thickness of the plate, this is not the case for the transverse stresses. This can be seen from an examination of suitable contour plots for the two stress states (Figures 10(a) and (b)). For the transverse stress at the centerline, the model predicts a change in sign from compressive at the top surface to tensile at the center of the plate. At a distance of 5 mm from the centerline, the transverse stresses are tensile on the top surface and compressive at the center of the plate. It is clear that the transverse stresses vary in a complicated manner and that the gage dimensions used are significant when compared with the distances over which the transverse stresses vary. It is likely that the neutron diffraction technique, as practiced here, has a spatial resolution that is insufficient for detection of changes in the transverse stresses through the plate thickness in this particular weld; it is possible, therefore, that some measure of the through-thickness–averaged transverse stress has been determined. There are other potentially significant causes of

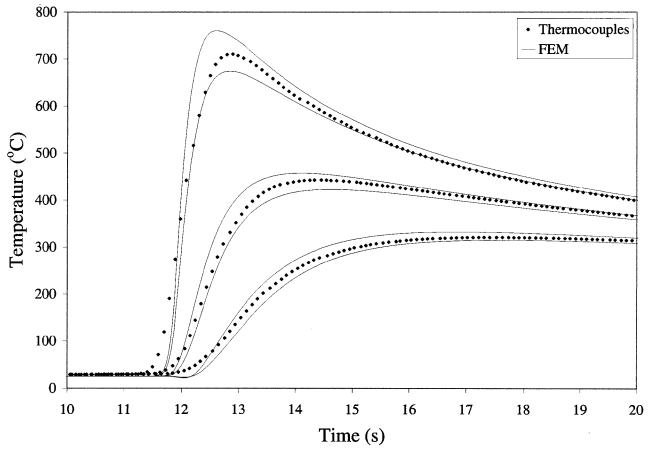

(*a*)

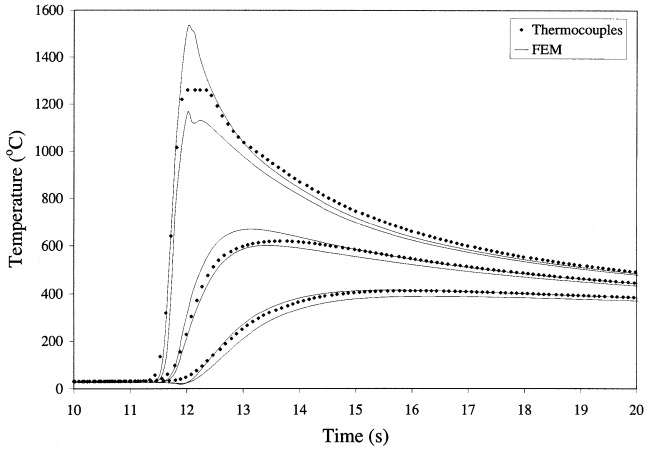

(*b*)

Fig. 8—Thermal cycles obtained from the thermocouple measurements and the numerical model for the testpiece welded at (*a*) +0 mA and (*b*) −40 mA defocus. The computed curves assume an uncertainty of ±2 mm in the position of the thermocouple.

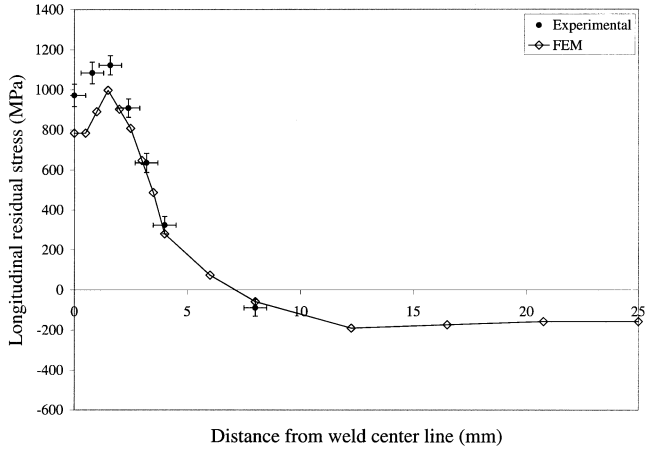

(*a*)

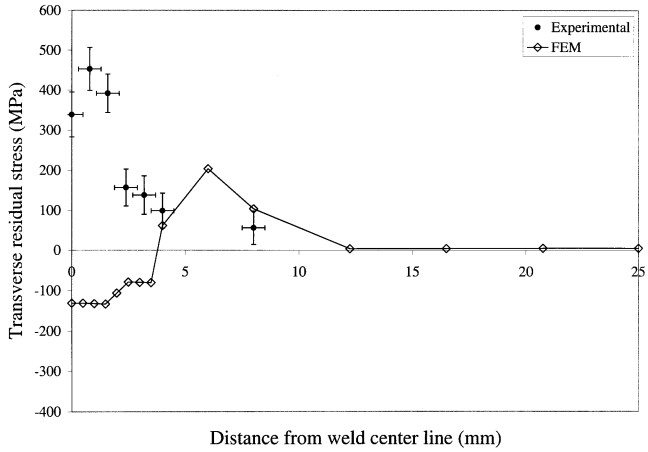

(*b*)

Fig. 9—Plots of the variation of the (*a*) surface longitudinal and (*b*) transverse residual stresses at the plate center, with distance away from the weld centerline.

error in the experimental technique, and these are discussed further in the Appendix.

During the course of the present work, the variation of the states of longitudinal and transverse stress with beam defocus has been evaluated with the computer model. In all cases, it has been found that the contour maps were similar in form to those presented in Figure 10, with more pronounced assymmetry with respect to depth being observed as the beam is defocused.

2. *Comparison of measured and predicted distortions*

The measured angular distortion, which was characterized by the butterfly angle, as described in Section III–C, increased in a small but detectable fashion from the start of each weld to its finish. Typical data are shown in Figure 11(a), in this case, for the weld fabricated at a +20 mA defocus. In this instance, the measured angular distortion is of the order of 1 deg; the predicted values are shown for comparison. The computed distortion is of the order of one-half of the measured value, and this remains approximately constant along the weld, although there are small end-effects. In fact, it has been found that the measured angular distortion varied systematically with beam defocus and to an extent

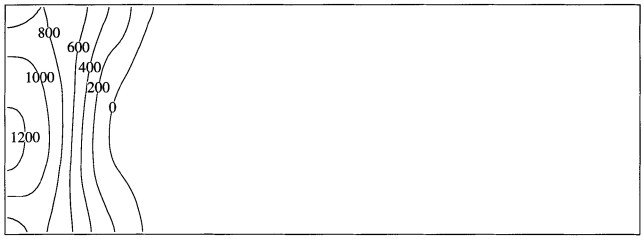

(*a*)

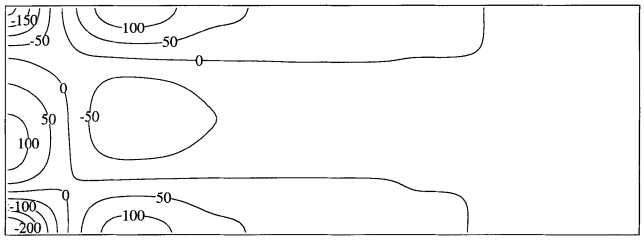

(*b*)

Fig. 10—Contour plots of the predicted residual stresses at the center of the plate welded at +20 mA defocus: (*a*) longitudinal stresses and (*b*) transverse stresses.

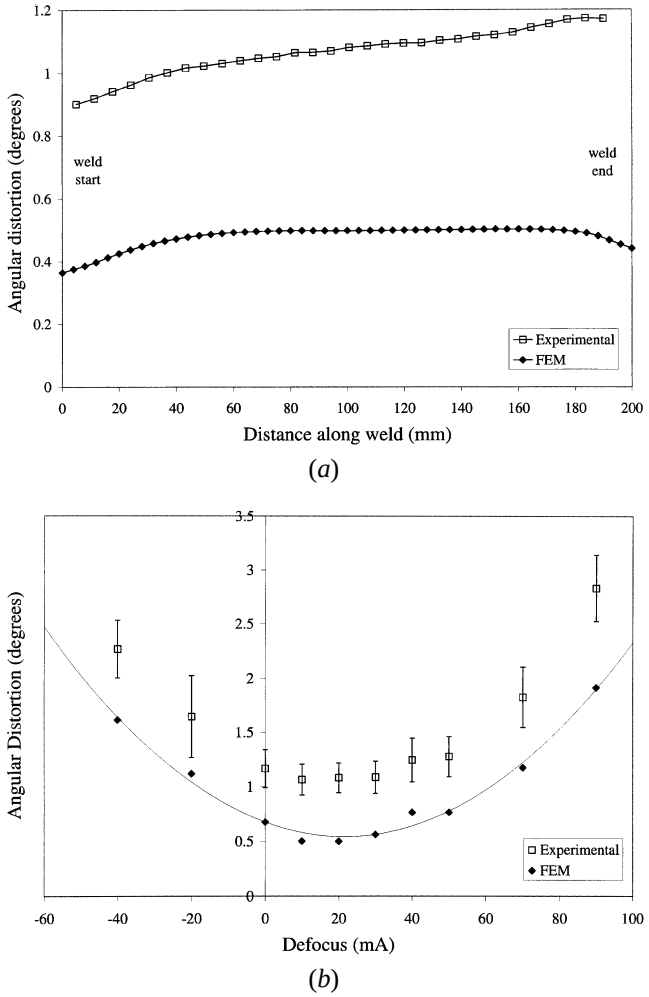

Fig. 11—(*a*) Plot of the observed and computed variation of the angular (butterfly) distortion along the length of the testpiece welded at +20 mA and (*b*) variation of observed and computed angular distortion with beam defocus.

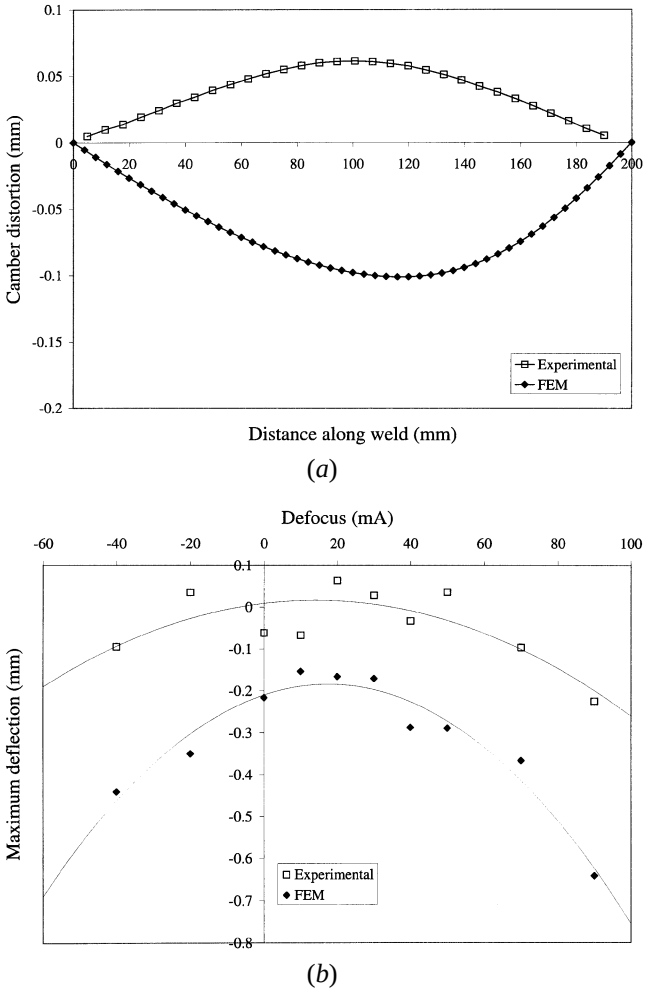

Fig. 12—(*a*) Plot of the observed and computed variation of the camber distortion for the testpiece welded at +20 mA and (*b*) variation of observed and computed maximum camber deflection with beam defocus.

that was large compared to the range of distortion observed along any given plate (Figure 11(b)). The condition of minimum distortion was achieved with a slightly overfocused beam; as the magnitude of the defocus is varied from this condition, the angular distortion increases concomitantly, with the largest distortions being observed for the nonpenetrating welds. This behavior arises because fusion profiles of an increasingly assymmetrical shape were produced, *i.e.*, more material is then melted above the neutral axes of the testpieces than below it. The effect on the angular distortion is reasonably well reproduced by the model, although the predictions are consistently smaller than the experimental values.

A plot of the measured and predicted camber distortion of the plate fabricated at +20 mA is presented in Figure 12(a). While the magnitude of the cambering observed for this weld is approximately correct, the sense is opposite that observed. This situation might have been anticipated since, at the normal focus condition, the energy is deposited more or less uniformily through the thickness of the plate; indeed, in the limit of uniform heat deposition, the sense of the cambering is, in fact, indeterminate because of the symmetry condition that is then implied. It has been found that the experimental data reflect this (Figure 12(b)). Particularly in the vicinity of the normal focus condition, the sense of cambering can be of either sign. The computational model predicts in all cases that the center of the weld sinks, *i.e.*, dish-shaped welds are produced, and this is indeed consistent with the experimental data far from the condition of normal focus. In contrast to the results for the angular mode, here the model systematically overpredicts the extent of distortion.

The evidence presented here suggests that the model is capable of predicting the extent of distortion, at least to a first approximation. The angular and cambering modes of distortion are, of course, dependent on each other, and this represents a plausible explanation for the discrepancy between theory and experiment. The model underpredicts the angular distortion, so that the model is then less resistant to cambering than it should be; consequently, the cambering is overpredicted. It is possible that a more exact description of the distortion could be achieved by tampering with the parameters of the thermal model. This could be done, but, given the methodology employed, this does not seem to be a reasonable thing to do at this stage, since the thermal model is in agreement with all the experimental data.

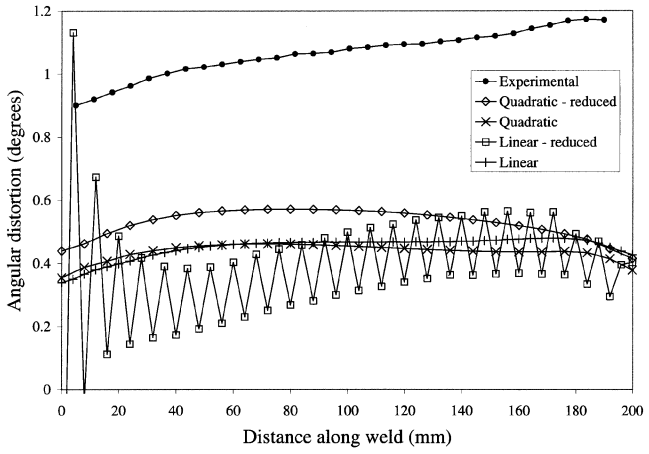

(*a*)

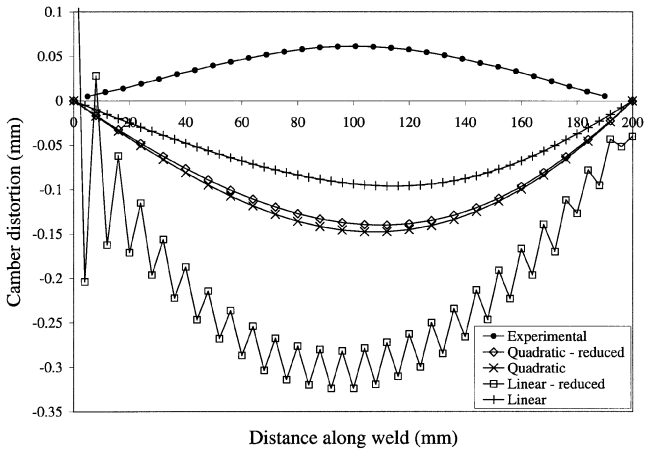

(*b*)

Fig. 13—Calculations of the extent of (*a*) angular distortion and (*b*) camber distortion made using different types of finite element, with and without reduced integration. Simulations for the weld fabricated at +20 mA defocus.

VI. ON THE SENSITIVITY OF THE RESULTS TO THE MESHES USED

It is well known that the successful implementation of the FEM requires the choice of a suitable and adequate mesh. In this section, emphasis is placed on evaluating the sensitivity of the predictions to (1) the type of elements used and (2) the number of elements in the mesh.

A. *The Element Types for the Mechanical Analysis*

A series of mechanical analyses were performed using linear and quadratic elements both with and without reduced integration. All meshes had eight elements through the thickness of the plate. The weld manufactured at +20 mA was chosen for this first study. The camber and angular distortions predicted to occur along the length of the weld are given in Figures 13(a) and (b), respectively. The experimental data are also shown.

Some thought needs to be given to whether the cambering or angular distortion represents the best test for the model. Here, it has been observed that the angular distortion is generated within a narrow region containing the weld and HAZ. This extends a distance of approximately 5 mm from the weld centerline; within this region, the mesh contains about ten columns of elements. If the resultant angular distortion of approximately 0.4 deg is assumed to occur by identical shear deformations in each of these columns, the required shear angle in each element is ~0.04 deg. In contrast, similar considerations indicate that the camber distortion has been captured with a considerably smaller shear angle in each element, approximately 0.003 deg. These considerations indicate that it is the angular distortion that represents the best test of the adequacy of the mesh.

Completely unsatisfactory results were obtained from the analyses that used linear elements and reduced integration. Oscillations on the scale of the elements arose along the complete length of the weld (Figure 14), due to the hourglassing effect (*e.g.*, Reference 39), which arises as a consequence of the inability of these elements to resist shear deformation. This situation is to be avoided, and, for this reason, the use of this type of element and integration procedure was abandoned at an early stage of the project.

For the angular distortion, the values obtained using linear elements were generally smaller than those obtained from the use of quadratic elements. By their nature, linear elements are incapable of distortion by pure bending and instead must accommodate any such deformation by shearing; the result is an overly stiff response that has been termed "shear locking."[41] With quadratic elements, the shape functions allow the element to undergo pure bending so that shear locking is avoided; nonetheless "volumetric locking" can occur, and it is known that this can be ameliorated using reduced-integration schemes.[41] Thus, the results presented in Figure 13 are consistent with the known behavior of the various elements. The closest agreement between the analyses and the experimental measurements is provided by the model run with quadratic elements and reduced integration. For this reason, quadratic elements with reduced integration were chosen for the analyses presented elsewhere in this article.

B. *On the Adequacy of the Mesh Employed*

The second study involved studying the variations in the distortions produced as the number of elements through the thickness of the mesh was varied from 4 to 12. Consistent with the previous study, quadratic elements with reduced integration were employed. As before, the testpiece welded at a +20 mA defocus was considered. The predicted angular and camber distortions are presented in Figures 15(a) and (b), respectively. The experimental data are also shown.

As anticipated, the degree of distortion was found to be sensitive to the extent of mesh refinement. In the case of cambering, the magnitude of the calculated distortion increased with the number of elements through the thickness, with evidence that an asymtotic limit was being reached when meshes with greater than eight elements through the thickness were employed. For reasons discussed in Section V–B, the sense is opposite that observed. For the angular distortion, all the results were within a band of ±0.1 deg from 0.4 deg at the start of the weld and 0.5 deg toward the center of the weld. While these results are significantly smaller than those obtained experimentally, increased degrees of discretization did not provide any further improvement in this agreement.

It was, therefore, concluded that eight elements represents

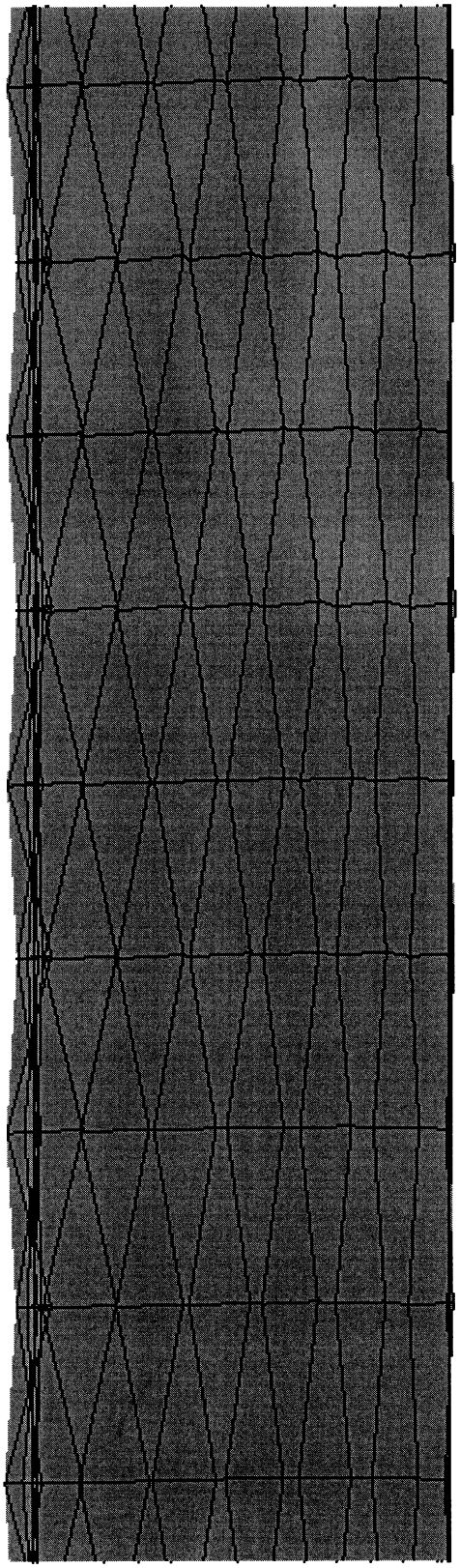

Fig. 14—Part of the mesh from the simulation of the +20 mA weld, illustrating the hourglassing effect.

the minimum acceptable number of elements required through the thickness of the testpiece. Consequently, all models were conducted with this level of discretization.

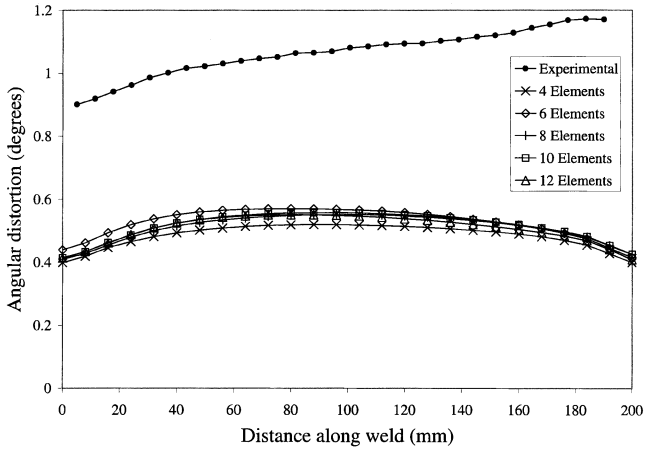

(*a*)

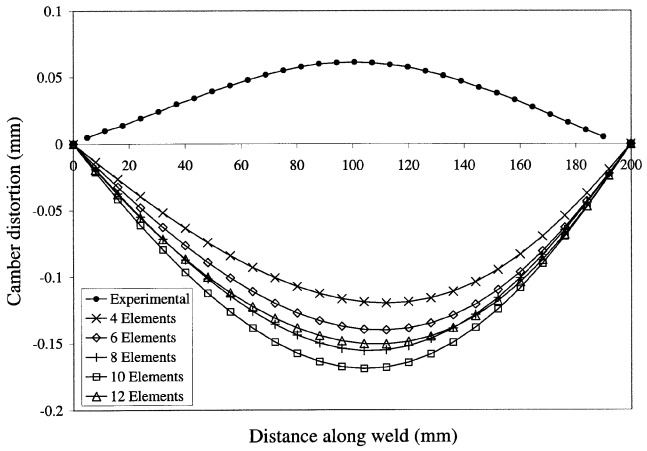

(*b*)

Fig. 15—Variation of the extent of (*a*) angular distortion and (*b*) camber distortion as a function of the number of elements used to discretize the through-thickness direction. Simulations for the weld fabricated at +20 mA defocus.

VII. CONCLUSIONS

The implementation of a numerical model for the prediction of the distortion arising from the electron-beam welding of WASPALOY has been described. The following conclusions can be drawn.

1. The longitudinal residual stresses predicted by the numerical model are in reasonable agreement with those obtained experimentally. On the centerline, the stresses are largest at the center of the plate and are of a magnitude equivalent to the yield stress or slightly beyond it. In the HAZ, there is little variation of the longitudinal stresses with distance through the plate; this is because the heat is deposited more or less uniformly through the thickness of the testpiece.
2. There exists a discrepancy between the experimentally determined transverse stresses and those computed from the model. It is suggested that the neutron diffraction technique, as practiced here, has a spatial resolution that is insufficient to characterize the transverse-stress field, since the stresses are small and because the transverse-stress field changes sign both through the thickness and with distance from the centerline.

3. The angular distortion generated by this welding process shows a systematic variation with the extent of defocus of the electron beam; the minimum distortion condition is achieved with a slight overfocusing of the beam. These effects were reproduced by the model, although the extent of angular distortion was consistently underpredicted by up to a factor of 2.
4. Far from the condition of normal focus, the sense of cambering was predicted correctly, although its extent was consistently overpredicted. It is possible that this is because the angular distortion is underpredicted, so that the plate is not resistant enough to bending in the cambering mode. At the condition of normal focus, the cambering was of indeterminate sense, as expected, since the energy is then deposited uniformly through the thickness of the workpiece.
5. It is emphasized that considerable care must be exercised in the creation of a suitable mesh for such analyses. The choice of element type in the mechanical analysis has been shown to have a pronounced effect upon the distortion predicted.
6. Despite the limitations identified, we believe that this kind of process model is capable of providing a useful first estimate of the levels of distortion and residual stresses to be anticipated during electron-beam welding.

ACKNOWLEDGMENTS

This work was sponsored by Rolls-Royce plc and the Defence Evaluation and Research Agency (Farnborough). One of the authors (HJS) acknowledges financial support in the form of a CASE award from the Engineering & Physical Sciences Research Council (EPSRC). The support of Paul Spilling, Steve McKenzie, Douglas Crooke, and Bridget Glassey (Rolls-Royce) and Mike Winstone and George Harrison (DERA) is appreciated. Helpful discussions over a number of years with Moyra McDill, Alan Oddy, and John Goldak, Carleton University, (Ottawa, Canada) are acknowledged.

APPENDIX
Note on the residual stress measurements

When attempting to determine residual stresses by the neutron diffraction technique, the reader should be aware that a number of difficulties may be encountered, which may, in some circumstances, lead to considerable uncertainties in the measurements. The following represents a summary of the pertinent points.

(1) There is always an uncertainty associated with identifying the location of the gage volume with respect to the geometry of the specimen, *i.e.*, the walls of the plate. Usually, this is achieved by monitoring the change in the integrated intensity of the diffraction peak as the sample is stepped into the neutron beam. However, a precise determination of the wall position may be difficult to achieve in practice due to the extended nature of the gage volume, which has the effect of making the wall appear diffuse. From experience, a conservative estimate of the error resulting from this effect is one-quarter of the width of the gage volume, *i.e.*, ± 0.5 mm for the measurements reported in this article.

(2) The gage volume has a finite volume. Consequently, the diffraction peaks from which the residual stress is determined receive contributions from material present in an extended volume. Provided that the intensity of the scattered beam is uniform across the gage volume and the stress state varies as a monotonic function of distance, the resultant residual stress obtained may be expected to be a volume-averaged measurement over the gage volume. However, for samples with sizeable textures, high attenuation with depth, or large stress gradients, this assumption may be invalid.

(3) The lattice strains from which the estimates of residual stress state are derived[21] are determined relative to a strain free lattice parameter. Changes in the composition of the phases present within the heat-affected and fusion zones may lead to the variation of this parameter in the region being scanned, and systematic errors can be accumulated in this way.

(4) One needs to be sure that the residual stresses that are deduced are representative of the bulk or engineering (type I) stresses. In some circumstances, it is possible to measure a superposition of the type I stresses and the type II microstresses, which are present on the scale of the microstructure. For WASPALOY, this effect has been studied in some detail.[22,23]

REFERENCES

1. H. Schultz: *Electron Beam Welding*, Abington Publishing, Cambridge, United Kingdom, 1993.
2. D.E. Powers, J.D. Ferrario, G.K. Hicken, J.F. Hinrichs, J.O. Milweski, and T.M. Mustaleski: in *The Welding Handbook*, R.L. O'Brien, ed., American Welding Society, Miami, FL, 1991, vol. 2, pp. 672-711.
3. *ASM Handbook*, D.L. Olson, T.A. Siewert. S. Liu, and G.R. Edwards, eds., ASM INTERNATIONAL, Materials Park, OH, 1993, vol. 6.
4. J.F. Lancaster: *The Physics of Welding*, 2nd ed., Pergamon Press, New York, NY, 1986.
5. N.O. Okerblom: *The Calculations of Deformation of Welded Metal Structures*, HMSO, London, 1958 (translated from Russian by L.R. Ronson).
6. O.W. Blodgett: *Design of Welded Structures*, The James F. Lincoln Arc Welding Foundation, Cleveland, OH, 1966.
7. S.J. Maddox: *Fatigue Strength of Welded Structures*, The Welding Institute, Cambridge, United Kingdom, 1969.
8. J. Lancaster: *Handbook of Structural Welding*, Abington Publishing, Cambridge, UK, 1992.
9. H. Nukumori: *Weld. Int.*, 1986, vol. 34, pp. 47-52.
10. D.E. Powers and G.R. LaFlamme: *Weld. J.*, 1988, vol. 67, pp. 25-31.
11. T. DebRoy and S.A. David: *Rev. Modern Phys.*, 67, pp. 85-112 (1995).
12. J.M.J. McDill, A.S. Oddy, and J.A. Goldak: in *International Trends in Welding Science and Technology*, S.A. David and J.M. Vitek, eds., ASM INTERNATIONAL, Materials Parks, OH, 1993.
13. *Trends in Welding Research*, H.B. Smartt, J.A. Johnson, and S.A. David, eds., ASM INTERNATIONAL, Materials Park, OH, 1996.
14. *Mathematical Modeling of Welding Phenomena 4*, H. Cerjak and H.K.D.H. Bhadeshia, eds., The Institute of Materials, London, 1997.
15. Y. Arata: *Plasma, Electron and Laser Beam Technology, Development and Use in Materials Processing*, ASM, Metals Park, OH, 1986.
16. P.S. Wei and W.H. Giedt: *Welding J.*, 1985, vol. 64, pp. 251s-259s.
17. N. Postacioglu, P. Kapadia, M. Davis, and J. Dowden: *J. Phys.—D: Appl. Phys.*, 1987, vol. 20, pp. 340-45.
18. M.J. Bibby, G. Burbridge, and J.A. Goldak: *Welding J.*, 1975, vol. 58, pp. 253-58.
19. J.F. King, S.A. David, J.E. Sims, and A.M. Nasreldin: *Welding J.*, 1986, vol. 65, pp. 39-47.
20. T.M. Mustaleski, R.W. McCaw, and O.E. Sims: *Welding J.*, 1988, vol. 67, pp. 53-59.
21. H.J. Stone, S.M. Roberts, P.J. Withers, T.M. Holden, and R.C. Reed: *Metall. Mater. Trans.*, 1999, vol. 30A, pp. 1797-1808.

22. H.J. Stone, T.M. Holden, and R.C. Reed: *Acta Mater.*, 1999, vol. 47, pp. 4435-48.
23. H.J. Stone, T.M. Holden, and R.C. Reed: *Scripta Mater.*, 1999, vol 40, pp. 353-58.
24. M.R. Daymond, M.A. Bourke, R.B. Von Dreele, B. Clausen, and T. Lorentzen: *J. Appl. Phys.*, 1997, vol. 82, pp. 1554-62.
25. J.A. Goldak, A. Oddy, M. Gu, W. Ma, A. Mashaie, and E. Hughes: *Mechanical Effects of Welding*, IUTAM Symp., L. Karlsson, L.E. Lindgren, and M. Jonsson, eds., Springer-Verlag, New York, NY, 1992, pp. 1-30.
26. J.M.J. McDill, A.S. Oddy, and J.A. Goldak: in *Int. Trends in Welding Science and Technology*, S.A. David and J.M. Vitek, eds. ASM INTERNATIONAL, Materials Park, OH, 1993.
27. A.S. Oddy, J.M.J. McDill, and J.A. Goldak: *J. Pressure Vessel Technol.*, 1990, vol. 112, pp. 309-11.
28. L. Karlsson and L.-E. Lindgren: in *Modeling of Casting, Welding and Advanced Solidification Processes V,* M. Rappaz *et al.*, eds. TMS, Warrendale, PA, 1991.
29. L. Wikander, L. Karlsson, M. Nasstrom, and P. Webster: *Modelling Simulation Mater. Sci. Eng.*, 1994, vol. 2, pp. 845-64.
30. L. Lindgren and L. Karlsson: *Int. J. Num. Meth. Eng.*, 1988, vol. 25, pp. 635-55.
31. J.B. Leblond, J. Devaux, and J.C. Devaux: *Int. J. Plasticity*, 1989, vol. 5, pp. 551-72.
32. J.B. Leblond, G. Mottet, and J.C. Devaux: *Journal of the Mechanics & Physics of Solids*, 1986, vol. 34, pp. 395-409.
33. J.M. Bergheau, D. Pont, and J.B. Leblond: in *Mechanical Effects of Welding*, IUTAM Conf. Proc., L. Karlsson, L.E. Lindgren, and M. Jonsson, Springer-Verlag, New York, NY, 1992.
34. J.H. Argyris, J. Szimmat, and K.J. Willam: *Computer Methods Appl. Mech. Eng.*, 1982, vol. 33, pp. 635-66.
35. *SYSWELD+ Finite Element Software*, Systus International, Paris.
36. H.J. Stone: Ph.D. Thesis, The University of Cambridge, Cambridge, United Kingdom, 1999.
37. See, for example, *Adv. Mater. and Processes* 1999, vol. 156, pp. 77-87.
38. D. Rosenthal: *Trans. ASME*, 1946, vol. 68, pp. 846-66.
39. J.A. Goldak, A. Chakravarti, and M. Bibby: *Met. Trans. B*, 1984, vol. 15B, pp. 299-305.
40. J.A. Goldak, M. Bibby, J. Moore, R. House, and B. Patel: *Metall. Trans. B*, 1986, vol. 17B, pp. 587-600.
41. O.C. Zienkiewicz and R.L. Taylor: *The Finite Element Method: Solid and Fluid Mechanics, Dynamics and Non-Linearity*, 4th ed., McGraw-Hill, Berkshire, England, 1994.